



## The sintering behavior of ellipsoidal particles

**Bjørk, R.**

*Published in:*  
Journal of the American Ceramic Society

*Link to article, DOI:*  
[10.1111/jace.18580](https://doi.org/10.1111/jace.18580)

*Publication date:*  
2022

*Document Version*  
Publisher's PDF, also known as Version of record

[Link back to DTU Orbit](#)

*Citation (APA):*  
Bjørk, R. (2022). The sintering behavior of ellipsoidal particles. *Journal of the American Ceramic Society*, 105(10), 6427-6436. <https://doi.org/10.1111/jace.18580>

---

### General rights

Copyright and moral rights for the publications made accessible in the public portal are retained by the authors and/or other copyright owners and it is a condition of accessing publications that users recognise and abide by the legal requirements associated with these rights.

- Users may download and print one copy of any publication from the public portal for the purpose of private study or research.
- You may not further distribute the material or use it for any profit-making activity or commercial gain
- You may freely distribute the URL identifying the publication in the public portal

If you believe that this document breaches copyright please contact us providing details, and we will remove access to the work immediately and investigate your claim.

## RESEARCH ARTICLE

# The sintering behavior of ellipsoidal particles

**R. Bjørk**

Department of Energy Conversion and Storage, Technical University of Denmark - DTU, Lyngby, Denmark

**Correspondence**

R. Bjørk, Department of Energy Conversion and Storage, Technical University of Denmark - DTU, Anker Engelunds Vej 1, DK-2800 Kgs. Lyngby, Denmark.  
Email: [rbj@dtu.dk](mailto:rbj@dtu.dk)

**Abstract**

The sintering behavior of ellipsoidally shaped particles, particularly spheroids, was studied using a numerical kinetic Monte Carlo model for solid-state sintering. Compact packings of spheroids with five different aspect ratios from 0.5 to 2.0, thus comprising oblate, spherical, and prolate particles, were generated by simulating the pouring of such particles into a cubic container. For each spheroid particle aspect ratio, five different packings were generated to provide statistics on the sintering properties. The sintering behavior was quantified by the densification rate, relative density, anisotropic strain, grain size, and grain coordination number, as determined from the kinetic Monte Carlo model. The spherical particles were found to sinter to a relative density of 0.87 before grain growth occurs, whereas the oblate and prolate particles reach a relative density of 0.91 before grain growth sets in, with the prolate particles sintering slightly better compared to oblate particles. The more extreme the particle aspect ratio, the more anisotropic the strain is. Finally, the oblate and prolate spheroids have a slightly higher mean grain coordination number and a slightly higher initial relative density compared to the spherical particles.

**KEYWORDS**

coordination number, densification, microstructure, modeling/model, sinter/sintering

## 1 | INTRODUCTION

Sintering of powder compacts is a key technological process in the manufacturing of ceramic and metal components for both existing and future technologies. For the latter, for example, solid oxide fuel cells (SOFCs) and solid oxide electrolysis cells (SOECs) are produced using sintering of various novel ceramic or metal powders.<sup>1–3</sup>

For a sintered powder compact, the degree of densification changes, for example, the percolation depth, mechanical strength, and electrical and thermal conductivity of the final product. The sintering behavior can

be controlled by a number of parameters external to the powder compact itself, such as sintering temperature, time, atmosphere, and application of load or an external field, but the internal properties of the powder compact also greatly influence its sintering behavior. These internal properties are, for example, pore formers, particle size distribution, and particle shapes. Among the internal parameters, the influence of pore formers<sup>4–6</sup> and particle size distribution<sup>7–13</sup> has been studied extensively and for the latter, it is well known that powders with a narrow particle size distribution sinter to higher relative density.

This is an open access article under the terms of the [Creative Commons Attribution-NonCommercial-NoDerivs](https://creativecommons.org/licenses/by-nc-nd/4.0/) License, which permits use and distribution in any medium, provided the original work is properly cited, the use is non-commercial and no modifications or adaptations are made.

© 2022 The Authors. *Journal of the American Ceramic Society* published by Wiley Periodicals LLC on behalf of American Ceramic Society.

However, the influence of the shape of the powder particles on the microstructural evolution and the final properties of a powder compact has not been studied in detail. The reason for this is most likely that although it is easy to add pore former particles to a powder compact or to sieve the powder before sintering to control the particle size distribution, the shape of powder particles is not as easy to control. However, with increasingly advanced powder production techniques, complex-shaped ceramic powder particles can now be produced,<sup>14</sup> and thus, it is scientifically interesting to understand how exactly the particle shape influences sintering behavior and microstructural properties.

The particle shape most studied in sintering, besides spherical particles that are the basis of countless studies, is ellipsoidal particles. Experimentally, the sintering behavior of ellipsoidal or spheroidal particles has been investigated for Cu and compared to flaky powders.<sup>15</sup> The sintering of ellipsoidally shaped  $\beta$ -Ga<sub>2</sub>O<sub>3</sub> particles has also been studied experimentally and compared to rod-shaped particles as well as a commercial powder.<sup>16</sup> The finding was that the ellipsoidal and rod-shaped particles had a higher sintering activity compared to the commercial powder. The sintering of ellipsoidal particles of LaPO<sub>4</sub> has also been investigated experimentally,<sup>17</sup> and results showed that the powder can be sintered to very high relative density (98%) with a balanced grain growth.

The sintering of ellipsoidal particles has also been studied using various modeling approaches. The sintering behavior as a function of the aspect ratio of the powder particles has been studied, with the finding that higher aspect ratio particles sinter to a higher density.<sup>18</sup> An analytical model based on Coble's two-sphere model<sup>19</sup> for the sintering of two ellipsoidal bodies (as well as polyhedral bodies) has also been derived.<sup>20</sup> Here, it was found that BaTiO<sub>3</sub> grains as observed using SEM could be approximated by ellipsoids of different sizes and orientations and that the model could be used to provide a good correlation between structural/geometrical and kinetics/physical parameters for this material. However, no analysis of the microstructure's evolution was given. Finally, the viscous sintering behavior of ellipsoidal particles has been investigated in the limit by modeling the shape evolution of an axisymmetric ellipsoidal particle by viscous flow driven by capillarity using a finite element model.<sup>21</sup> The results showed that the sintering force can most likely be determined from experiments by observing the change in the length of the semiminor axis of the particle during sintering. This work was a continuation of a previous work also studying the viscous sintering of an ellipsoidal particle using the virial method applied to Stokes equation.<sup>22</sup> It is also of interest to mention that the sintering behav-

ior of ellipsoidal pores has also been considered in the literature.<sup>23,24</sup>

The consensus in the literature is that ellipsoidal particles seem to be able to sinter to a high relative density, but the mechanism for this has not been clarified. Similarly, a directly comparison with spherical particles has not been performed, and only a single study has attempted to clarify the sintering behavior as a function of particle aspect ratio. The objective of the work presented here is to study in detail the effect of the particle shape on sintering, so that an understanding of the densification and microstructural evolution behavior can be gained. To achieve this understanding, we simulate the microstructural evolution during sintering of powder compacts consisting of spheroids, that is, ellipsoids with two of the semiaxis equal to each other. For these, the single parameter defining their shape is their aspect ratio or eccentricity and their sintering behavior can thus easily be characterized as a function of this parameter. We simulate the sintering of powder compacts consisting of thousands of particles of the specified shape to allow the microstructure to be characterized in detail continuously throughout the sintering process. The simulation is performed using a kinetic Monte Carlo (kMC) model of sintering that incorporates all the materials processes necessary to simulate simple solid-state sintering.<sup>25</sup> In this model grain growth and grain and pore shape changes can be studied, unlike in discrete element models (DEMs)<sup>12</sup>, and many more particles can be simulated compared to using a surface evolver approach.<sup>26</sup>

## 2 | THE NUMERICAL MODEL

To simulate sintering, we here employ a 3D statistical-mechanical kMC model, which has previously been used extensively to simulate the sintering behavior of powders.<sup>13,18,27–30</sup> In the kMC model, the microstructure is represented on a discretized cubic grid, that is, a voxel grid, as an ensemble of material particles. A voxel site can either contain a material particle or be empty, and thus, microstructural features such as grains, pores, grain boundaries, and pore surfaces can be resolved.

The physical processes occurring during simple solid-state sintering are all present in the model, such as curvature-driven grain growth with the drag force of pinning but mobile pores, pore migration by surface diffusion, vacancy formation at pore surfaces with vacancy concentration given by the Gibbs–Thomson relation, grain boundary diffusion of the vacancies, and vacancy annihilation at grain boundaries. The technical details of the model can be found in Refs. [25, 31]. Here, we will consider free sintering with no constraining forces, although the latter can also be included in the kMC modeling framework.<sup>32</sup>

During a sintering simulation, the evolution of the system, which is driven by a minimization of the total interfacial free energy, is determined through a number of kMC processes. The interfacial free energy in the model is simply quantified by the number of unlike neighbors a given voxel site has, as a cubic grid is considered. The model then simulates sintering by a number of processes that manipulate the ensemble of material particles. Surface and grain boundary diffusion are simulated by randomly exchanging two neighboring sites. Grain growth is simulated by changing the membership of a grain boundary material particle from one grain to another. Finally, densification by vacancy annihilation is simulated by collapsing a column of sites from an isolated pore site at a grain boundary to the surface of the sample.<sup>33</sup>

The standard kMC approach of driving the system is used. If a randomly chosen process at a randomly chosen voxel lowers the total energy of the system, then the given “move” is accepted. If the energy is increased, the move is accepted with a probability calculated using the standard Metropolis algorithm. As model parameters, the grain boundary and pore surface energies can be controlled, as can the diffusion rates through the attempt frequencies of the different processes. These parameters must be chosen to match the desired simulated sintering conditions. However, this is not trivial in the kMC model, as the model is inherently nondimensional. The length scale of the model is linearly proportional to real length. Time in the model is measured in Monte Carlo step (MCS), where one MCS has passed when the number of attempted grain growth moves equals the total number of grain sites in the system. Time measured in MCS is linearly related to real time,<sup>25</sup> with the proportionality factor depending on the chosen length scale of the model. By comparing the densification behavior of a kMC model to a similar experimental system, for example, the sintering of copper spheres as observed using X-ray tomography,<sup>25</sup> or the sintering of fuel cell materials,<sup>29,30</sup> nickel,<sup>28</sup> or stainless steel<sup>34</sup> as observed using FIB-SEM the model parameters can be related to physical parameters. The model has also been used to study the sintering of close-packed spheres<sup>27</sup> where the model confirmed and expanded previously reported experimental results.

The simulation parameters used here are temperature for grain growth and pore migration of  $k_B T_{PM} = k_B T_{GG} = 1$  and for vacancy formation of  $k_B T_{VA} = 15$ . The attempt frequencies were chosen in the ratio 1:1:1 for grain growth, pore migration, and vacancy formation, respectively. Similar temperatures have previously been used to model the sintering of packed spheres with different particle size distributions,<sup>13</sup> and these values display a realistic sintering behavior for a powder compact. Similar values were also used by Ref. [34] who used temperatures of  $k_B T_{PM} = k_B T_{GG} = 1$  and for vacancy formation of  $k_B T_{VA} = 13$  and

attempt frequencies of 1:1:1 in the study of spark plasma sintering (SPS) of stainless steel 304 L. Similar values were used by Ref. [29], specifically  $k_B T_{GG} = 1.16$ ,  $k_B T_{PM} = 1.48$ , and  $k_B T_{VA} = 37$  and frequency attempts of 3.4:1:1 as obtained using artificial neural networks (ANNs) by training these on a kMC simulation of the sintering of microstructures of  $\text{La}_{0.6}\text{Sr}_{0.4}\text{Co}_{0.2}\text{Fe}_{0.8}\text{O}_3$  as determined from scanning electron microscopy (FIB-SEM) reconstruction. For simulating the sintering of submicron nickel powders attempt frequencies of 0.2:1:1 and temperatures of  $k_B T_{GG} = 0.5$ ,  $k_B T_{PM} = 1.5$ , and  $k_B T_{VA} = 13$  were used.<sup>28</sup> These parameters resulted in an accurate prediction of the 3D microstructure evolution of the sintering of nickel at the submicron scale. Thus, there is a broad agreement that the values chosen in this study result in a realistic sintering behavior.

## 2.1 | Generating the powder compact

The initial condition for the sintering simulation is a packing of spheroidal particles, which here was generated using the framework described in Ref. [35]. Using this framework, it is possible to simulate the pouring of spheroidal particles into a container, and simulate the settling of these under the influence of gravity. This mechanism is similar to previously used approaches to generate initial powder packings,<sup>13</sup> except there only spherical particles were considered. Although additional driving forces such as liquid solvents, surfactants, pressure, and applied field can influence the packing of powder particles, gravity is arguably the simplest driving force to consider. Regular packings of ellipsoidal particles have also been considered,<sup>36</sup> and could perhaps be interesting to study in the future, similar to the way the sintering behavior of close-packed spheres has been studied.<sup>27</sup>

During the initial powder packing simulation, the particles are simulated in full 3D and cannot thus overlap. As mentioned previously, we here only consider spheroidal particles, to reduce the parameter space invested. A spheroid is characterized by its aspect ratio,  $ar$ , which is defined as the ratio between the two semiaxis of the spheroid,  $c$  and  $a$ , respectively, that is,  $ar = c/a$ . Spheroids with an aspect ratio ( $ar = c/a < 1$ ) are oblate, whereas spheroids with an aspect ratio ( $ar = c/a > 1$ ) are prolate. We consider spheroids with an aspect ratio of 0.5, 0.75, 1, 1.5, and 2, respectively. The particles are poured into a cubic container with equal side lengths. The powder particles were chosen such that the individual particles all had the same volume. This also means that the particles have varying surface areas. Compared to the sphere, the oblates with an aspect ratio of 0.5 and 0.75 have a surface area that is larger by a factor of 1.10 and 1.02, respectively, whereas the prolates with aspect ratio 1.5 and 2 have a

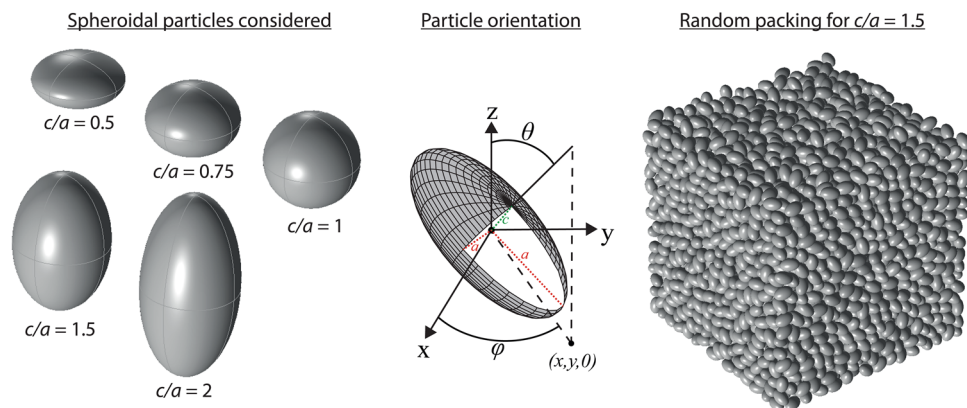


**FIGURE 1** The semiaxes,  $a$  and  $c$ , and the spherical orientation angles for an oblate spheroid. In spherical coordinates,  $\phi$  denotes the azimuthal angle and  $\theta$  denotes the polar angle. A random packing of 4783 spheroids with  $c/a = 1.5$  is also shown

surface area that is larger by a factor of 1.03 and 1.08, respectively.

For each particle aspect ratio, five different packings were generated to calculate a statistical uncertainty on the computed properties. The average number of particles in a cube sample is  $4713 \pm 144$  across all packings considered. Figure 1 shows a packing of spheroidal particles with an aspect ratio of 1.5 as well as the individual spheroids considered in this study. Once the initial powder packing has been generated, this is then discretized on a three-dimensional grid with a resolution of  $300 \times 300 \times 300$ , so as to be evolved using the kMC modeling sintering framework.

As mentioned previously, the sintering of ellipsoidal particles has been studied as a function of the aspect ratio of the powder particles.<sup>18</sup> However, in this study, the powder compact was generated through a simulated uniaxially compressing, which is different from the method employed here. As will be discussed subsequently, this has an influence on the sintering behavior observed from the powder.

The density of the packing varies at the bottom and top of the box, due to the effect of pouring in the particles, but stabilizes to a constant value at 16% of the box length from either the bottom or top surface. Thus, the density is homogeneous with the central 68% of the sample. Therefore, the analysis of the sintering dynamics is only considered within this central homogeneous area of the sample, where the density gradient effect, as well as surface effects of the sample, can be disregarded, as will also be discussed subsequently.

## 2.2 | Initial particle orientation

When the particles are poured into the cube container, their orientation in space will not be random, but will align

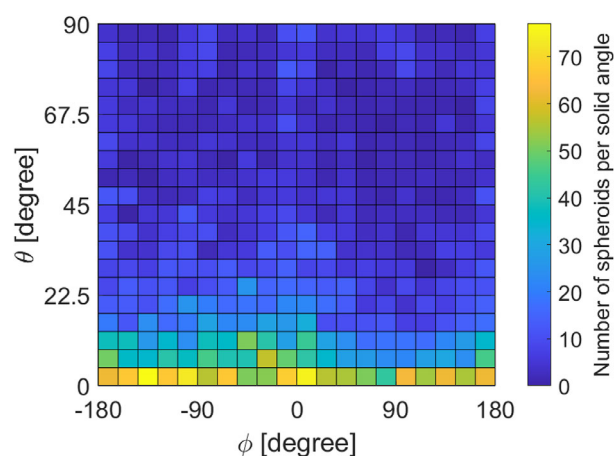


**FIGURE 2** The distribution of the orientation of the  $c$ -axis in a poured random packing of spheroidal particles with an aspect ratio of 0.5. There is a total of 4684 particles in the packing

to the flat bottom surface of the cube. Consider, for example, the first layer of spheroids that is poured into the cube container. These will naturally align themselves to the flat bottom surface of the container, that is, an oblate will lay flat in the bottom surface. When additional particles are then poured into the container, these will also naturally align themselves relative to the layers of the spheroids below them.

We can characterize this in terms of the spherical coordinate angles, where  $\phi$  denotes the azimuthal angle and  $\theta$  denotes the polar angle of the  $c$ -axis of the spheroid, as also shown in Figure 1. For the example above with an oblate aligning to the flat bottom surface of the cube, we have  $\theta = 0$  and the additional layers of oblates above will have  $\theta \approx 0$ . The angle  $\phi$  will be randomly distributed.

In Figure 2, the distribution of the spherical coordinate angles  $\phi$  and  $\theta$  is shown for an initial powder packing with spheroid particles with an aspect ratio of 0.5. As can be seen from the figure, the tendency discussed above that the

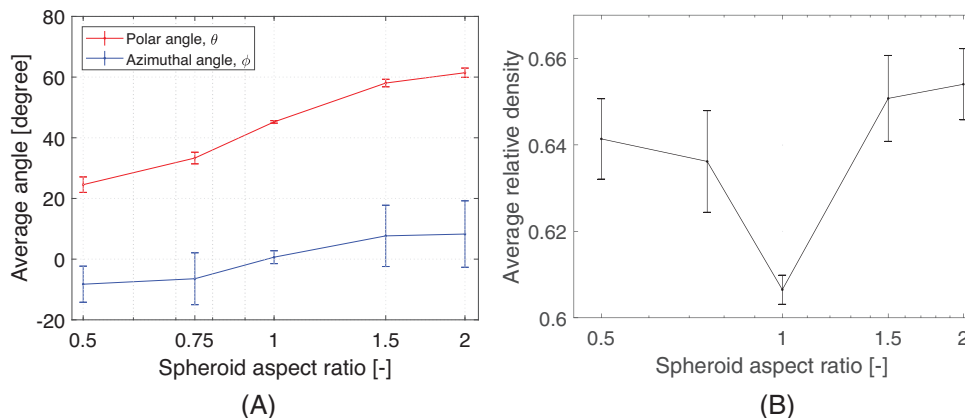


**FIGURE 3** (A) The average orientation of the spheroidal particles with respect to the spherical polar angle,  $\theta$ , and the spherical azimuthal angle  $\phi$ , as a function of the aspect ratio of the spheroidal particles and (B) the average relative density as a function of the particle aspect ratio

oblate particles will orient with respect to the flat bottom surface, that is,  $\theta \approx 0$ , is clearly seen.

To quantify this orientation of the spheroidal particles for all the investigated aspect ratios, we have computed the average orientation in the azimuthal direction,  $\phi$ , and the polar direction,  $\theta$ , as a function of the particle aspect ratio. As stated above, we consider five different packings for each aspect ratio. The results are shown in Figure 3(A). As can be seen, the average orientation in the polar direction,  $\langle\theta\rangle$ , clearly depends on the particle aspect ratio due to the behavior described above. This will be important to keep in mind when the sintering behavior of the particles is discussed subsequently, as it directly influences the surface area contact between particles. Note that the polar and azimuthal angles are somewhat meaningless for spheres, that is, when the spheroid aspect ratio is 1. However, the values of the polar and azimuthal angles do vary continuously as a function of the aspect ratio of the spheroids, and the values for the sphere can be seen as the limiting values when the aspect ratio of the spheroids approaches 1 for both increasing and decreasing aspect ratio. Finally, we also investigate the relative density of the initial powder packing as a function of the particle aspect ratio. This is shown in Figure 3(B). The relative density is given for the internal homogeneous part of the sample only, as will be detailed in the next section. It is seen that the variation is small, and furthermore, the values are consistent with previously published values,<sup>35</sup> where the relative density of spheroid packing also increases when the aspect ratio deviates from spherical.<sup>37</sup>

### 3 | SINTERING BEHAVIOR

We simulate an isothermal sintering process for the different powder packings considered. For each sintering simulation, the microstructure is characterized in terms of

relative density, grain size, and grain coordination number every 2500 MCS steps. All simulations have been run for 60 000 MCS steps, except the spherical particle packings, which was run for 80 000 MCS steps, which is enough to reach a high relative density state. As discussed above, to only consider the homogeneous part of the sample and to ignore surface effects near the edge of the packings, the microstructural properties were only analyzed in the central homogeneous part of the sample simulated, which here is a box with a side length of 68% of the full box side length, centered on the center of the packing. Only grains fully inside this volume are considered in the calculated grain properties, such as grain size and grain coordination number. As mentioned previously, for each particle aspect ratio considered, five different powder samples were generated and their sintering behavior modeled. In the following results, the average property is taken across these five samples for each aspect ratio. This allows statistical uncertainties to be shown for the examined properties of the system, such as relative density or grain size.

In Figure 4, the average relative density as a function of the number of MCS steps is shown for the different packings, with the error bar indicating the standard deviation between the five packings with the same spheroid aspect ratio. As can be seen from the figure, the spheroidal particles densify faster than the spherical particles, but the trend is also that the particles with an extreme aspect ratio sinter faster than those closer to spheroidicity.

To get a more visual understanding of the sintering behavior, we show in Figure 5 a slice through five different packings with different particle aspect ratios for four different sintering times. The slice is through the middle of the packing at  $y = 150$  voxels. As can be seen from the figure, the grains for the extreme aspect ratios at the same time MCS step clearly appear larger. This will be discussed subsequently.

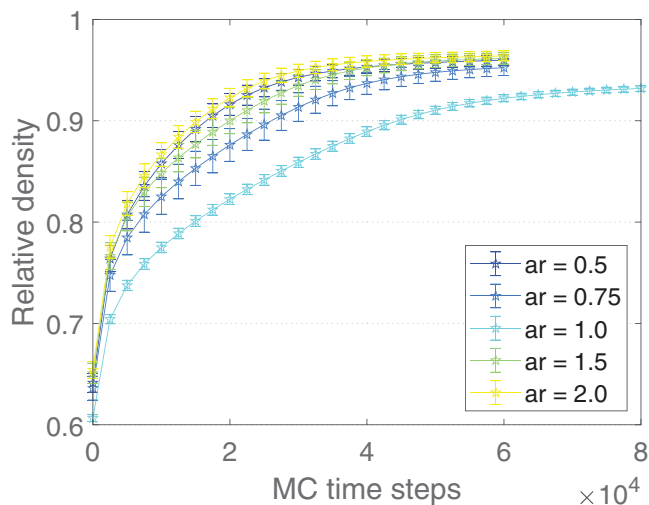


FIGURE 4 The average relative density as a function of the number of Monte Carlo time steps taken for the different packings

### 3.1 | Relative density and grain size evolution

The above analysis considered only the relative density and not the grain growth in the powder compact during den-

sification. To quantify this, we define the average grain size in terms of the equivalent radius, which is the radius a spherical particle of the corresponding volume would have. This is defined as  $r_{\text{equi}} = (\frac{3}{4\pi}V)^{1/3}$ , where  $V$  is the volume of a particle. The average grain size is shown as a function of the relative density in Figure 6 for all particle aspect ratios. For purely spherical powders with a normalized particle size distribution, it has also been observed that powders with the widest distribution sinter to a lower relative density.<sup>13</sup> One can see from the figure that the particles with aspect ratios different from 1 sinter to a higher relative density before grain growth sets in. This effect is most likely caused by the higher surface to volume ratio of the spheroidal particles compared to the spherical particles, but also potentially the anisotropic particle packing demonstrated earlier, as will be discussed subsequently. To reflect upon Figure 5, the reason the packings with extreme aspect ratios display large grains is because, as shown in Figure 4, these more quickly, that is, at a lower MCS step, obtain a high relative density and this, as shown in Figure 6, results in an increased grain growth being reached at a lower MCS step.

Ref. [18] also investigated the sintering behavior as a function of the aspect ratio of the powder particles, and

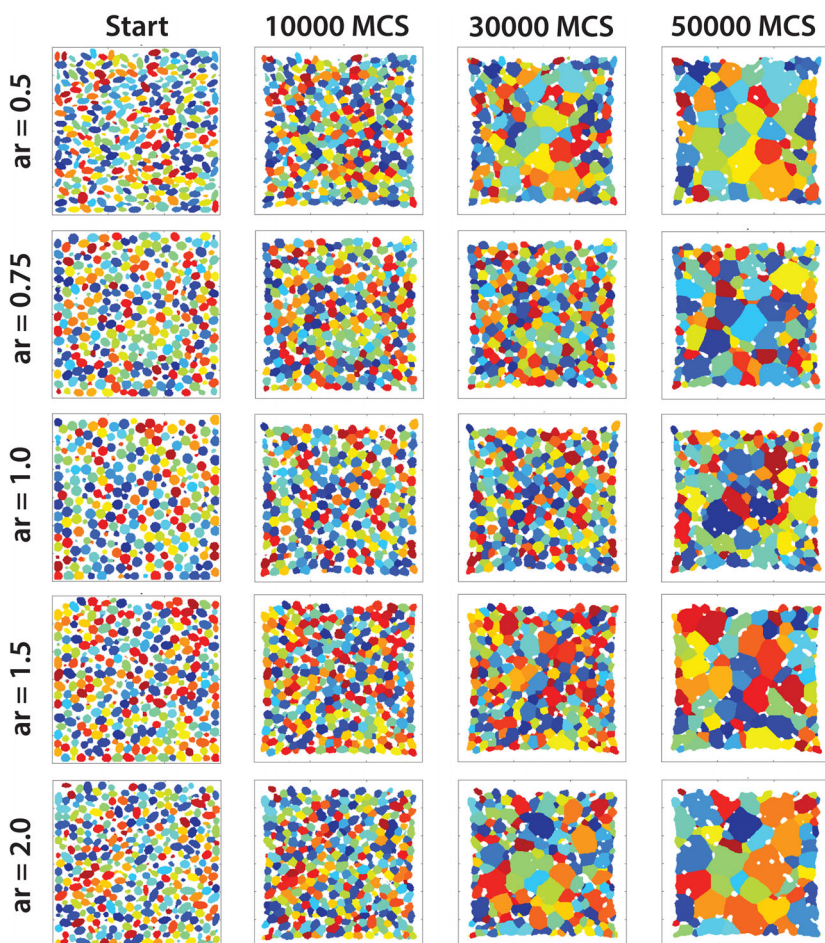
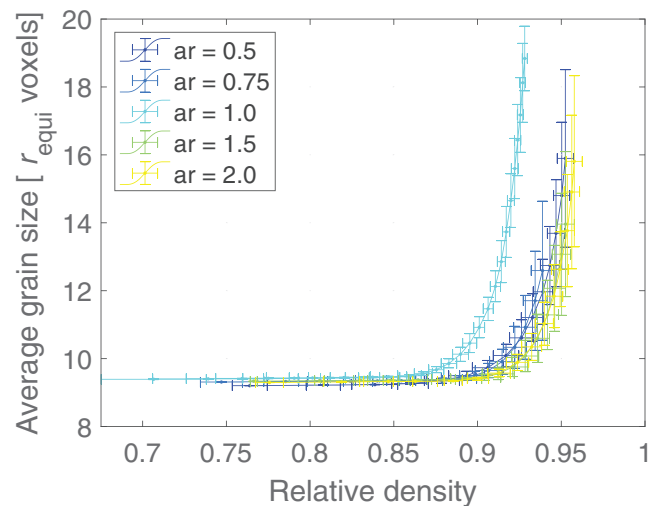


FIGURE 5 A slice of different powder packings, characterized by their aspect ratio, for different MCS steps. The slice is through the  $xz$ -plane for  $y = 150$  voxels



**FIGURE 6** The average grain size, in terms of equivalent radius, that is, the radius of a sphere having the same volume as the respective grain,  $r_{\text{equi}}$ , as a function of relative density for the different particle aspect ratios

similarly to this study, they also find that higher aspect ratio particles sinter to a higher density. However, they find a weaker dependence on aspect ratio than determined here. However, in Ref. [18], the initial powder compact is not generated through a pouring of particles into a container but rather by generating a very loose random packing with a relative density of 0.1 and then uniaxially compressing this to a relative density of 0.55–0.57. This results in a powder packing where the particles do not orient to the surface of the container, as is the case in this study. This, in turn, means that the contacting surface area in the study of Ref. [18] will be lower than in this study, as the particles here are more aligned, as evident in Figures 2 and 3(A). This better alignment of the particles results in the better sintering behavior found here.

### 3.2 | Anisotropic sintering

As was discussed in the section on the properties of the packings, the spheroidal particles have a preferred orientation in space. This means that both the particles have a higher contact surface area, but also potentially that the pore network in the packings could be asymmetric, which can lead to anisotropic sintering.<sup>38</sup> To study this, we consider the strain of the packings while sintering. The strain in the  $x$ - and  $y$ -direction should be identical as a result of the pouring of the particles, and this has been verified numerically to also be the case. In Figure 7, the ratio of the strain in the  $x$ - and  $y$ -directions,  $\epsilon_{xy}$ , to the strain in the  $z$ -direction,  $\epsilon_z$ , is shown. It is noted that for the packings with spherical particles, the strain ratio is not exactly equal to 1, due to particles sticking out of the sample at the top surface

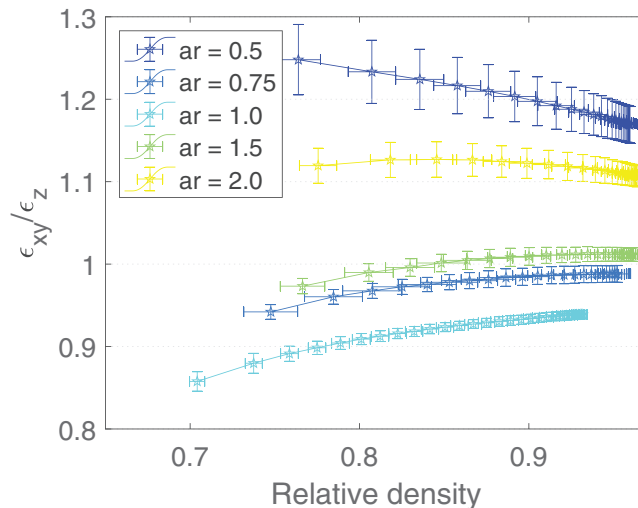


**FIGURE 7** The ratio of the strain in the  $x$ - and  $y$ -direction,  $\epsilon_{xy}$ , to the strain in the  $z$ -direction,  $\epsilon_z$ , as a function of relative density

because of the pouring mechanism, resulting in a uneven surface<sup>33</sup> and the fact that packing resulting from pouring can have a small anisotropic vertical orientation due to gravity.<sup>39</sup> As can be seen from Figure 7, the more extreme the aspect ratio of the particles, the more the strain ratio deviates from the isotropic sintering of the packings with spherical particles. The strain in the  $x$ - and  $y$ -directions is much larger than that in the  $z$ -direction for the extreme aspect ratios because the touching surface area of the particles is more aligned to the  $z$ -direction, meaning that there is less shrinkage in this direction as the sample sinters.

Anisotropic sintering, specifically with respect to the strain rate, has also been observed in both experiments and simulations<sup>40</sup> for samples that have been partially sinter-forged prior to sintering. Although this is not exactly the case studied here, the packing of particles with gravity will also, as argued above, lead to anisotropic packings, akin to pressed samples. In the sinter-forging study, it was found that the anisotropic sintering behavior is dominated by the anisotropic contact area distribution rather than by the anisotropic coordination number. Furthermore, only a very small anisotropy was observed in the pore network, using a linear intercept method. Using the identical method on the voxel data described in this work also revealed no discernable difference in the  $x$ -,  $y$ -, and  $z$ -directions in the pore network, that is, no anisotropy in the pore network similarly to Ref. [40].

### 3.3 | Distribution parameters during sintering

The sintering behavior can also be examined by investigating the number of grains present in the central part of the sample, as sintering progresses. In a previous work, we

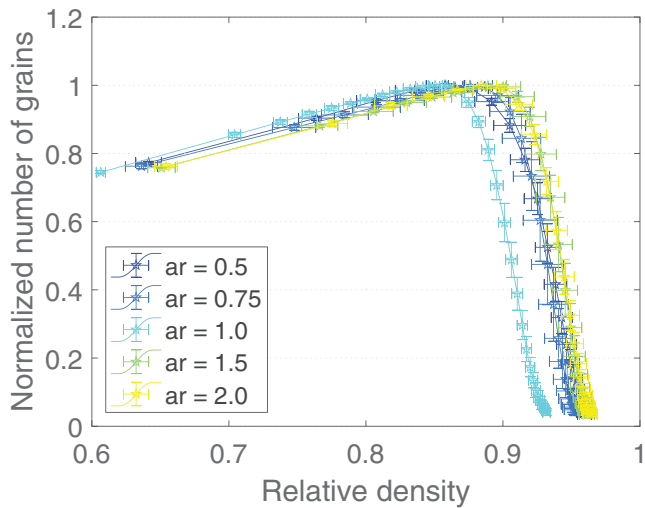


**FIGURE 8** The normalized number of grains in a given powder packing as a function of the relative density for the different aspect ratios

investigated the number of small grains in a given sample, but this is a meaningless quantity for a powder where all particles are identical initially. Thus, here we consider all particles, regardless of size. Initially, each particle is a single grain, and thus, the number of grains equals the number of particles in the investigated central part of the cube sample.<sup>13</sup> The normalized number of grains as a function of relative density is shown in Figure 8, that is, the number of grains in the central part of the cube has been normalized to the maximum number of grains present in the central part at any time during the sintering process. As can be seen from the figure, the number of grains initially increases, which occurs because the sample as a whole is densifying. As the central part, where the microstructural parameters are investigated, is fixed in volume, more grains will be present in this volume as the sample densifies; thus, the normalized number of grains increases with relative density. However, when grain growths occurs, as evident from comparing Figure 6 with Figure 8, the number of grains decreases rapidly. Thus, the analysis of the number of grains in the given central part of the powder sample fully supports the evolution of the grain size with respect to the relative density that was discussed above.

### 3.4 | Grain coordination number

As also done in a previous study on the sintering behavior of spherical particles with a particle size distribution, it can be of interest to study how the contacts between grains evolve as sintering progresses, as this can also help explain the previously described sintering behavior. The number of contacts between grains is the grain coordination num-

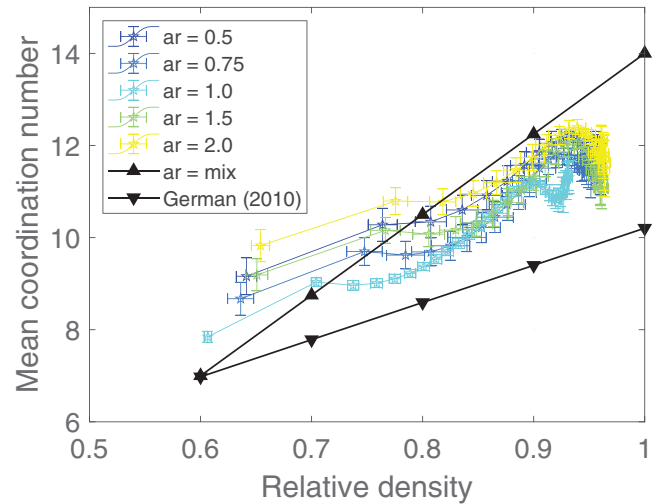


**FIGURE 9** The mean coordination number of the grains as a function of relative density

ber. This is also an interesting property to study, as Young's modulus, mechanical hardness, and fracture toughness are directly proportional to the mean grain coordination number in the initial stage of sintering.<sup>41</sup> The average value of the grain coordination number is shown in Figure 9 as a function of relative density for the different particle aspect ratios considered. Shown in the figure is also the relation for the coordination number as a function of relative density given by Refs. [42] and [43] for monosized spherical particles. Note that the data from the simulation are recorded at a fixed frequency, but the dynamics with respect to the relative density is faster in the initial part of the sintering. Therefore, the data points in the plots are not evenly distributed. However, this has little influence on the interpretation of the data, which is also found in a previous study; the analytical expressions under- and overestimate the mean coordination number as a function of relative density. The initial mean contact number for spheres is known from literature to be 6–7,<sup>39,44</sup> and the slightly higher initial mean coordination number reported here is due to the kMC segmentation of the spheres.

As can be seen from the figure, the mean grain coordination number increases with relative density as expected. However, the spherical particles have a slightly lower mean coordination number compared to the oblate and prolate spheroids. Ref. [18] also mentions that powders with high aspect ratio particles also have a higher average coordination number, but do not quantify this statement. For the evolution in mean grain coordination number, we here see a much larger spread in coordination number at a given relative density compared to that seen for spherical particles with a given particle size distribution. For these latter powders, the evolution of the mean coordination number

was very similar, which is not the case for the samples considered here.

The effect that the mean grain coordination number increases with relative density can at low relative density be explained by the fact that the sample is densifying, bringing more grains in contact with each other. However, once grain growths set in, the grain size distribution changes from mono-sized, leading some grains to grow and others to shrink. It has been argued that this should cause the coordination number to increase, as there will be more large particles, which can have a large number of contacts.<sup>8,12</sup> However, we see that at the relative density where grain growths occurs, the mean coordination number decreases, as has also previously been observed,<sup>13,45,46</sup> and thus, does not follow the initially proposed trend.

## 4 | DATA STATEMENT

All data shown in this manuscript, that is, the kMC data sets as a function of time and the derived quantities such as relative density, are available from Ref. [47]. The data files for each simulation are around 200 Mb in compressed format.

## 5 | CONCLUSION

We have used a numerical kMC model to study the sintering behavior of ellipsoidally shaped particles, particularly spheroids, during solid-state sintering. Compacts of spheroids were generated numerically by simulated pouring of spheroidal particles into a cubic container. Spheroidal particles with five different aspect ratios were used, including oblate, spherical, and prolate particles. The sintering behavior quantified by the densification rate, relative density, grain size, and grain coordination number was determined from the Monte Carlo model for five different random packings for each spheroid aspect ratio. Both the oblate and prolate particles were found to sinter to higher relative densities before grain growth sets in compared to the spherical particles, with the oblate particles sintering slightly more poorly compared to the prolate particles. The strain in the packings was found to be anisotropic, due to the orientation of the particles resulting from the poured packing. The number of grains present in the sample as a function of relative density is also determined and shown to display the well-known behavior of first increasing up to a relative density of 0.85–0.9 after which it decreases as grain growth sets in. Finally, the grain coordination number is also shown to increase as a function of relative density. The improved

sintering behavior of the oblate and prolate spheroids can be explained from their anisotropic contact surface area, but effects such as their slightly higher mean coordination number and a slightly higher initial relative density compared to the spherical particles can also influence their sintering behavior.

## REFERENCES

1. Fukui T, Ohara S, Naito M, Nogi K. Performance and stability of SOFC anode fabricated from NiO–YSZ composite particles. *J Power Sources*. 2002;110:91–5.
2. Shikazono N, Sakamoto Y, Yamaguchi Y, Kasagi N. Microstructure and polarization characteristics of anode supported tubular solid oxide fuel cell with co-precipitated and mechanically mixed Ni-YSZ anodes. *J Power Sources*. 2009;193:520–40.
3. Marinha D, Dessemond L, Cronin JS, Wilson JR, Barnett SA, Djurado E. Microstructural 3D reconstruction and performance evaluation of LSCF cathodes obtained by electrostatic spray deposition. *Chem Mater*. 2011;23:5340–48.
4. Sanson A, Pinasco P, Roncari E. Influence of pore formers on slurry composition and microstructure of tape cast supporting anodes for SOFCs. *J Eur Ceram Soc*. 2008;28:1221–26.
5. Mingyi L, Bo Y, Jingming X, Jing C. Influence of pore formers on physical properties and microstructures of supporting cathodes of solid oxide electrolysis cells. *Int J Hydrogen Energy*. 2010;35:2670–74.
6. Feng Y, Wang K, Yao J, Webley PA, Smart S, Wang H. Effect of the addition of polyvinylpyrrolidone as a pore-former on microstructure and mechanical strength of porous alumina ceramics. *Ceram Int*. 2013;39:7551–56.
7. Patterson BR, Griffin JA. Effect of particle size distribution on sintering of tungsten. *Mod Dev Powder Metall*. 1985;15(4):279–88.
8. Yeh TS, Sacks MD. Effect of particle size distribution on the sintering of alumina. *J Am Ceram Soc*. 1988;71(12):484–7.
9. Shiau FS, Fang TT, Leu TH. Effect of particle-size distribution on the microstructural evolution in the intermediate stage of sintering. *J Am Ceram Soc*. 1997;80(2):286–90.
10. Ting JM, Lin RY. Effect of particle size distribution on sintering. Part I. Modelling. *J Mat Sci*. 1994;29(7):1867–72.
11. Ting JM, Lin RY. Effect of particle size distribution on sintering. Part II. Sintering of alumina. *J Mat Sci*. 1995;30(9):2382–89.
12. Wonisch A, Kraft T, Moseler M, Riedel H. Effect of different particle size distributions on solid-state sintering: a microscopic simulation approach. *J Am Ceram Soc*. 2009;92(7):1428–34.
13. Bjørk R, Tikare V, Frandsen HL, Pryds N. The effect of particle size distributions on the microstructural evolution during sintering. *J Am Ceram Soc*. 2013;96(1):103–110.
14. Stingaciu M, Eikeland AZ, Gjørup FH, Deledda S, Christensen M. Optimization of magnetic properties in fast consolidated SrFe<sub>12</sub>O<sub>19</sub> nanocrystallites. *RSC Adv*. 2019;9:12968–76.
15. Wu C-J, Cheng S-L, Sheng Y-J, Tsao H-K. Reduction-assisted sintering of micron-sized copper powders at low temperature by ethanol vapor. *RSC Adv*. 2015;5(66):53275–79.
16. Shan J-J, Li C-H, Wu J-M, Liu J-A, Chen A-N, Shi Y-S. Sintering behavior and microstructural evolution of the monodispersed  $\beta$ -gallium oxide micro-particles with different morphology and size. *Ceram Int*. 2017;43(18):16843–50.

17. Haiyan L, Jiachen L, Yufeng Z. Sintering and microstructure of LaPO<sub>4</sub> ceramic. *J Rare Earths*. 2005;23:142–44.
18. Yan Z, Hara S, Shikazono N. Effect of powder morphology on the microstructural characteristics of La<sub>0.6</sub>Sr<sub>0.4</sub>Co<sub>0.2</sub>Fe<sub>0.8</sub>O<sub>3</sub> cathode: a kinetic Monte Carlo investigation. *Int J Hydrogen Energy*. 2017;42(17):12601–14.
19. Coble RL. Effects of particle-size distribution in initial-stage sintering. *J Am Ceram Soc*. 1973;56:461–66.
20. Mitić VV, Paunović V, Pavlović VP, Živković Lj. Sintering process influence on microstructure and intergranular impedance of rare-earth modified BaTiO<sub>3</sub>-ceramics. *Sci Sintering*. 2011;43:277–87.
21. Katsura K, Shinoda Y, Akatsu T, Wakai F. Sintering force behind shape evolution by viscous flow. *J Eur Ceram Soc*. 2015;35:1119–22.
22. Wakai F, Shinoda Y, Akatsu T. Tensor-Virial equation for deformation of a particle in viscous sintering. *J Am Ceram Soc*. 2012;95(9):2785–87.
23. Olevsky EA, Kushnarev B, Maximenko A, Tikare V, Braginsky M. Modelling of anisotropic sintering in crystalline ceramics. *Philos Mag*. 2005;85(19):2123–46.
24. Kanchika S, Wakai F. Surface tension-pressure superposition principle for anisotropic shrinkage of an ellipsoidal pore in viscous sintering. *J Eur Ceram Soc*. 2018;38(12):4283–89.
25. Tikare V, Braginsky M, Bouvard D, Vagnon A. Numerical simulation of microstructural evolution during sintering at the mesoscale in a 3D powder compact. *Comp Mater Sci*. 2010;48(2):317–25.
26. Wakai F, Yoshida M, Shinoda Y, Akatsu T. Coarsening and grain growth in sintering of two particles of different sizes. *Acta Mater*. 2005;53(5):1361–71.
27. Bjørk R, Tikare V, Frandsen HL, Pryds N. The sintering behavior of close-packed spheres. *Scripta Mater*. 2012;67(1):81–84.
28. Hara S, Ohi A, Shikazono N. Sintering analysis of sub-micron-sized nickel powders: kinetic Monte Carlo simulation verified by FIB-SEM reconstruction. *J Power Sources*. 2015;276:105–12.
29. Yan Z, Kim Y, Hara S, Shikazono N. Prediction of La<sub>0.6</sub>Sr<sub>0.4</sub>Co<sub>0.2</sub>Fe<sub>0.8</sub>O<sub>3</sub> cathode microstructures during sintering: kinetic Monte Carlo (KMC) simulations calibrated by artificial neural networks. *J Power Sources*. 2017;346:103–12.
30. Yan Z, Hara S, Shikazono N. Towards a realistic prediction of sintering of solid oxide fuel cell electrodes: from tomography to discrete element and kinetic Monte Carlo simulations. *Scr Mater*. 2018;146:31–35.
31. Cardona CG, Tikare V, Plimpton SJ. Parallel simulation of 3D sintering. *Int J Comp Mat Sci Surf Eng*. 2011;4(1):37–54.
32. Bjørk R, Frandsen HL, Pryds N. Modeling the microstructural evolution during constrained sintering. *J Am Ceram Soc*. 2015;98:3490–95.
33. Bjørk R, Frandsen HL, Tikare V, Olevsky E, Pryds N. Strain in the mesoscale kinetic Monte Carlo model for sintering. *Comp Mater Sci*. 2014;82:293–97.
34. Sweidan FB, Ryu HJ. Kinetic Monte Carlo simulations of the sintering microstructural evolution in density graded stainless steel fabricated by SPS. *Mater Today Comm*. 2020;101863.
35. Zhou Z-Y, Zou R-P, Pinson D, Yu A-B. Dynamic simulation of the packing of ellipsoidal particles. *Ind Eng Chem Res*. 2011;50:9787–98.
36. Tsutsumi Y. Arrangements of uniformly sized particles in a powder bed. *Powder Technol*. 1973;7:181–88.
37. Donev A, Cisse I, Sachs D, Variano EA, Stillinger FH, Connelly R, et al. Improving the density of jammed disordered packings using ellipsoids. *Science*. 2004;303:990–93.
38. Okuma G, Miyaki R, Shinobe K, Sciazko A, Shimura T, Yan Z, et al. Anisotropic microstructural evolution and coarsening in free sintering and constrained sintering of metal film by using FIB-SEM tomography. *Acta Mat*. 2021;215:117087.
39. Nolan GT, Kavanagh PE. Computer simulation of random packing of hard spheres. *Powder Technol*. 1992;72:149–55.
40. Wonisch A, Guillon O, Kraft T, Moseler M, Riedel H, Rödel J. Stress-induced anisotropy of sintering alumina: discrete element modelling and experiments. *Acta Mater*. 2007;55:5187–99.
41. Boonyongmaneerat Y. Mechanical properties of partially sintered materials. *Mat Sci Eng A*. 2007;452:773–80.
42. Arzt E. The influence of an increasing particle coordination on the densification of spherical powders. *Acta Mat*. 1982;30(10):1883–90.
43. German RM. Sintering theory and practice. New York; Toronto: Wiley-Interscience, 1996.
44. Bezrukov A, Stoyan D, Bargieł M. Spatial statistics for simulated packings of spheres. *Image Anal Stereol*. 2001;20:203–6.
45. Suzuki M, Oshima T. Co-ordination number of a multi-component randomly packed bed of spheres with size distribution. *Powder Technol*. 1985;44:213–18.
46. Yang A, Miller CT, Turcoliver LD. Simulation of correlated and uncorrelated packing of random size spheres. *Phys Rev E*. 1996;53:1516.
47. Bjørk R. Data set for the sintering behavior of ellipsoidal particles. <https://doi.org/10.11583/DTU.19738789>

**How to cite this article:** Bjørk R. The sintering behavior of ellipsoidal particles. *J Am Ceram Soc*. 2022;105:6427–6436.  
<https://doi.org/10.1111/jace.18580>